

Duality between atomic configurations and Bloch states in twisted 2D bilayers.

Stephen Carr,¹ Daniel Massatt,² Mitchell Luskin,² and Efthimios Kaxiras^{1,3}

¹*Department of Physics, Harvard University, Cambridge, Massachusetts 02138, USA.*

²*School of Mathematics, University of Minnesota, Minneapolis, Minnesota, 55455, USA.*

³*John A. Paulson School of Engineering and Applied Sciences,
Harvard University, Cambridge, Massachusetts 02138, USA.*

(Dated: December 14, 2024)

The stacking of individual layers of two-dimensional (2D) materials can be experimentally controlled with remarkable precision on the order of 0.1° . The relative orientation of successive layers introduces variations in the electronic properties that depend sensitively on the twist angle, creating moiré super-lattices. Here, we use simple theoretical models and accurate electronic structure calculations to predict that the electronic density in stacked 2D layers can vary in real space in a manner that replicates features of the band-structure in momentum-space. In particular, we draw a link between these banded real space electronic structures and the complexity of exact $k \cdot p$ models in the same energy range for each material we studied. A direct consequence of the patterns is the localization of electronic states. We demonstrate this effect in graphene, a semi-metal, and MoSe₂, a representative material of the transition metal dichalcogenide family of semiconductors. This effect can be useful in the design of localized electronic modes, arising from layer stackings, for experimental or technological applications.

The number of two-dimensional (2D) materials that have been experimentally isolated as single-layers of atomic-scale thickness has been growing at a rapid pace^{1–6}. Alongside these advances, methods to combine single layers into multi-layer heterostructures have developed a remarkable level of control over the relative orientation of successive layers, on the order of 0.1° ^{7–10}. The resulting heterostructures represent a new type of composite materials with properties spanning a vast range that includes insulators, semiconductors, metals and superconductors¹¹. The different arrangements of layers of 2D materials provide an intriguing platform for exploring new physics and potential applications based on their electronic, optical, magnetic and thermal properties. The relative orientation of successive layers, often characterized by a twist angle between the ideal in-plane lattices, represents an additional “knob” for adjusting the system properties. A well-studied example is twisted bilayer graphene (tBLG), where the twist-angle between successive layers of graphene causes controllable inter-layer electronic hybridization: at certain magic-angles ($< 1.2^\circ$) a symmetric hybridization between the two Dirac cones from the individual layers introduces flat bands in the bilayer band-structure and results in highly-localized electronic states^{12–17}. In the present work we use simple models and accurate electronic structure calculations to predict that this twist-induced localization is a phenomenon common to many types of layered heterostructures and we suggest that this effect can result in interesting correlated electron behavior, as was recently observed at the magic-angles of tBLG¹⁰, or large-scale electronic arrays, as seen in heterogenous bilayer TMDC structures¹⁸.

Accurate calculations of the properties of layered structures that involve small twist angles is challenging because these atomic arrangements are either incommensurate or have periodicity over length scales

several orders of magnitude larger than the primitive unit cells of the individual layers. Large-scale Density Functional Theory (DFT) approaches, continuum models, or empirical tight binding models have been used to capture the physics^{19–22}. In tBLG, the Dirac cone yields a simple low-energy Hamiltonian from which momentum-scattering interactions between layers can be computed^{13,20,21,23,24}. For transition-metal dichalcogenide (TMDC) systems, similar models for the parabolic band-edges have been used²⁵. Here, we employ accurate *ab-initio* tight-binding hamiltonians derived from DFT and Maximally Localized Wannier Functions (MLWF)^{26,27} within a framework specifically developed for twisted 2D systems^{28,29}. This approach enables us to investigate the electronic features in arbitrarily twisted 2D materials without the need to develop low-energy effective theories, whose range of validity may be limited. With this method, we obtain the local density of states (LDoS) of aperiodic systems described by the *ab-initio* tight-binding hamiltonians by computing local spectral properties at the center of large circular regions that contain millions of atoms. To obtain the numerical results in this work, we use a 60 nm diameter for TMDCs and a 200 nm diameter for graphene. This is adequate to fully capture the properties of stacked layers with arbitrary relative twist angles.

To illustrate the main concepts, we focus on the twisted bilayer of MoSe₂ (tBLMS). Our choice is motivated by the fact that this material is representative of the family of TMDC’s, which exhibit rich behavior in terms of electronic, optical and excitonic properties. We choose the bilayer reference state to be the 2H MoSe₂ bulk system, where each atomic layer is rotated by 180° relative to the layers directly above and below it. The effects we describe are general and we have verified that they are manifested in other materials like graphene, as we discuss below. To simplify our discussion of the moiré

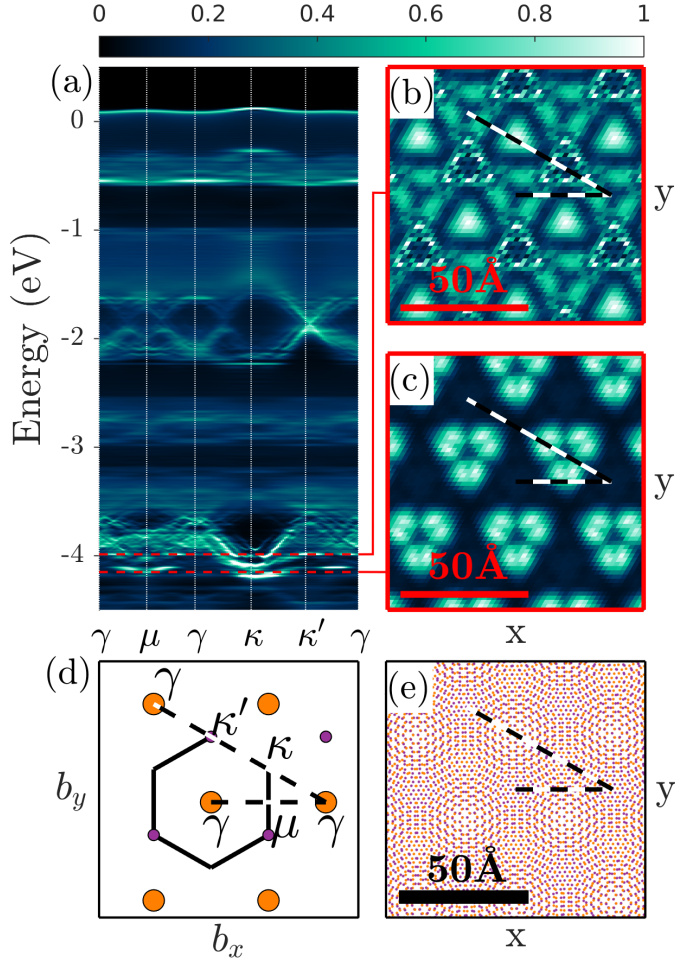


FIG. 1. (a) The p_z Local Density of States (LDoS) in 5° twisted bilayer 2H-MoSe₂ as a function of stacking configuration along the high-symmetry directions $\gamma \rightarrow \mu \rightarrow \kappa \rightarrow \kappa'$ shown in (d). Only the valence-band energy range is shown. (b,c) Top views of the LDoS over the moiré pattern at the two energies indicated by the dashed red lines in (a). (d) Top view of the bilayer MoSe₂ configuration space. A few unit cells of monolayer MoSe₂ are shown with Mo sites in purple and Se sites in orange and the high symmetry configurations are labeled. An effective “Brillouin zone” of configurations is outlined as the dark hexagon. (e) Top view of the atomic positions in the twisted bilayer; the dashed line shows the approximate path of sampled configurations over one copy of the moiré pattern.

physics, we ignore spin-orbit coupling and screening corrections, which can later be included in our formalism and are not expected to qualitatively affect the results. In Fig. 1 we show the LDoS intensity of the p_z orbitals of Se as a function of Fermi energy and local atomic structure; these orbitals extend the farthest out of the plane of the layer, and interact most strongly across the bilayer. In experimental microscopy studies, the most prominent features will arise from these atomic orbitals.

We also introduce in Fig. 1 an important concept

for exploring the physics, namely we display the LDoS for atomic structures chosen along lines in configuration space which connect high symmetry stackings in the bilayer at $\theta = 0^\circ$ twist. This is analogous to displaying band-structures in reciprocal (momentum) space along lines connecting high-symmetry points in the Brillouin Zone (BZ). The symmetry points of the local stacking in our example are labeled γ , μ , κ , and κ' , in direct analogy to the common labels for the symmetry points in the hexagonal BZ of MoSe₂ and other 2D materials with a 2D hexagonal Bravais lattice, which are commonly labeled Γ , M , K , and K' . Throughout this paper, we use Latin characters to represent features in the familiar picture of Bloch states and Greek characters for the analogous features in the dual picture based on the configuration (real)space.

Near the energy values of -4.0 eV, -2.0 eV, and -0.5 eV there exist smoothly varying features in the configuration-dependent LDoS. In Fig. 1(b,c), the real-space dependence of the LDoS shows interesting structures on the scale of the moiré pattern. In Fig. 2, we compare the features around -4.0 eV to the LDOS of bilayer graphene with and without twist. Near the central energy E_1 of this region, sharp angled lines are visible, and near the energy extrema E_2 flat line-segments corresponding to localized electronic states can be seen. The angled lines near E_1 can be interpreted as real-space band structures over configuration space, caused by an infinite lattice of coupled Bloch states. The smooth variations in LDoS can be attributed solely to the local variation in interlayer coupling over configuration space¹⁸, while the electronic localization and real-space bands depend on a coupling between these different local variations caused by a nonzero twist. For $\theta \neq 0^\circ$, the localized modes appear in both tBLG and tBLMS. Their appearance in tBLG at $\theta = 0.5^\circ$ agrees well with previous results on the second magic-angle localized wavefunction¹³; we have also previously verified that our model produces the first magic-angle localized state, near 1.1° ²⁹. By extension, we interpret $\theta = 5^\circ$ as being a magic-angle for tBLMS in the energy region near -4.0 eV. To demonstrate the localized nature of these electronic states, we show the spatial variation of LDoS for the corresponding energy in Fig. 2. The two systems show very similar patterns of localized electronic states but at different length scales, which are set by the moiré length of the corresponding magic-angles. This is the type of feature that scanning tunneling microscopy experiments would be able to detect, and they appear to be a common phenomenon in twisted bilayer materials.

The real-space bands near E_1 in the LDoS of tBLMS are absent in tBLG. To explain why these two systems share some features but differ in other important ways, we consider a simple 1D model consisting of two chains of single-atom unit cells with a starting lattice parameter of $L = 1$. The mismatch is introduced by changing the lattice spacing of one layer to λL , for some λ value close to 1 as shown in in Fig. 3(a). For the single-layer elec-

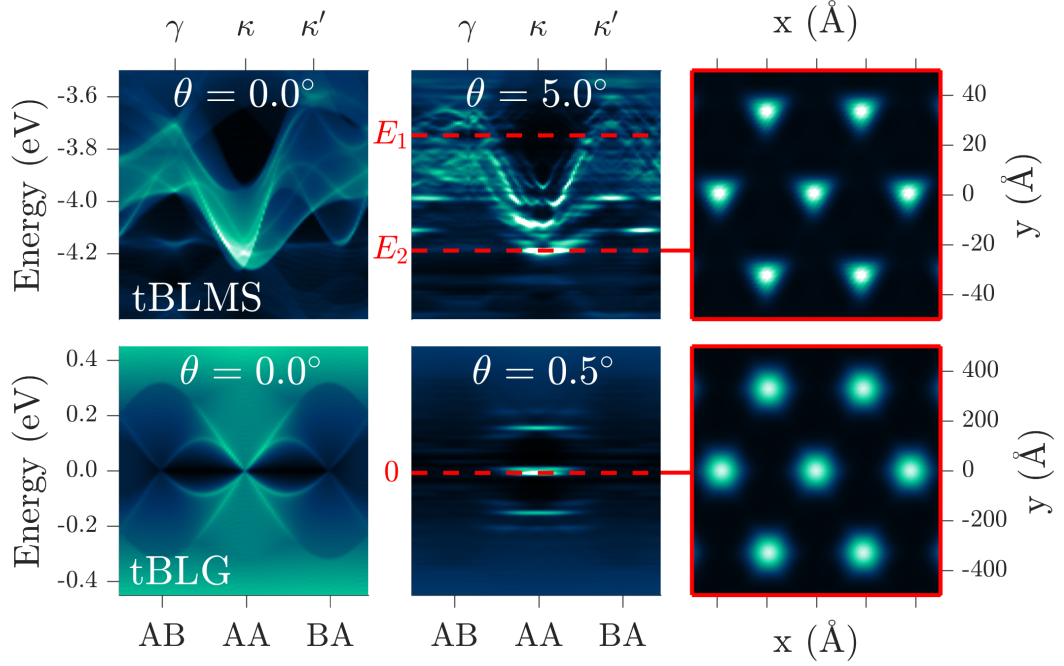


FIG. 2. Comparison of features in the local density of states (LDoS) for the tBLMS and tBLG systems at two different twist angles in each case (left and middle panels). The right panels show top views of the real-space variation in LDoS at the energy values identified by the horizontal dashed lines in each case.

tronic structure we use only a nearest-neighbor hopping of $T_0 = 1$ eV, while for two atoms in different layers separated by a distance d , the interlayer coupling is chosen to be

$$T(d) = T_1 \cos(\pi d) e^{-(2d)^3} \quad (1)$$

with all parameters in the same energy unit (eV). The exact form of $T(d)$ is not very important; it is chosen to mimic the features of the *ab-initio* interlayer coupling found earlier in BLG and BLMS^{26,27}. The real-space LDoS for this model with $\lambda = 100/92$ and different values for the interlayer coupling amplitude T_1 is shown in Fig. 3. We compute the LDoS here via the conventional method: diagonalizing a periodic supercell with 6 samples in the 1D Brillouin zone. Dispersionless modes appear for $T_1 > 0$, and the smooth band-like features appear for $T_1 > 2T_0$ (the representative cases $T_1 = T_0$ and $T_1 = 3T_0$ are shown).

We analyze the physics of this model in the context of $k \cdot p$ theory. For a perfect periodic bilayer, the Bloch states in layer 1 with momentum k can only couple to Bloch states in layer 2 with the same momentum value. Introducing a lattice mismatch between two layers, in the present case arising from $\lambda \neq 1$, causes off-diagonal coupling in the Bloch states between k and $k' \neq k$ momentum states. We consider how some starting Bloch state k with energy ϵ in layer 2 will couple to Bloch states in layer 1. The construction is shown in Fig. 3. The layer 1 Bloch states of momentum $k + nb_2$ (b_2 being the reciprocal-space

primitive vector of layer 2 and n an integer) are shifted back to the original BZ to help visualize the model. The coupling between Bloch states is given by the Fourier transform of T , $\hat{T}(q)$, evaluated at the scattering momenta nb_2 . The construction is repeated starting from the coupled layer 1 states, and using scattering momenta mb_1 , with b_1 the reciprocal-space primitive vector of layer 1 and m an integer. In this manner a lattice of coupled Bloch states is constructed. The only ingredient left to fully define an effective $k \cdot p$ hamiltonian is a suitable cut-off radius, that is, a maximum scattering distance K_{\max} such that the states which are outside the cut-off do not contribute strongly to the energy region of interest around ϵ . From a Green's function perspective, the relative connection between two Bloch states ψ_a and ψ_b with average energy $E_{ab} = (E_a + E_b)/2$ and relative scattering distance q_{ab} is expected to be $G_{ab}(E) \approx \hat{T}(q_{ab})/(E_{ab} - \epsilon)$: if the interlayer coupling $\hat{T}(q_{ab})$ is smaller than the energy difference between the average energy of these states and ϵ , the matrix element will be less than one. A sequence of such couplings that are less than one can therefore be neglected. As a result, only sequences of Bloch-states that are strongly coupled need to be included in the model. These are indicated in Fig. 3(c,e) as states within the black dotted lines. For large coupling amplitude T_1 , all Bloch states become coupled, resulting in very slow convergence in the cut-off-radius. In this case, the natural advantage of the $k \cdot p$ approach is lost, and there is no reduction in the size of the basis compared to the real-space tight-binding Hamiltonian (TBH). The

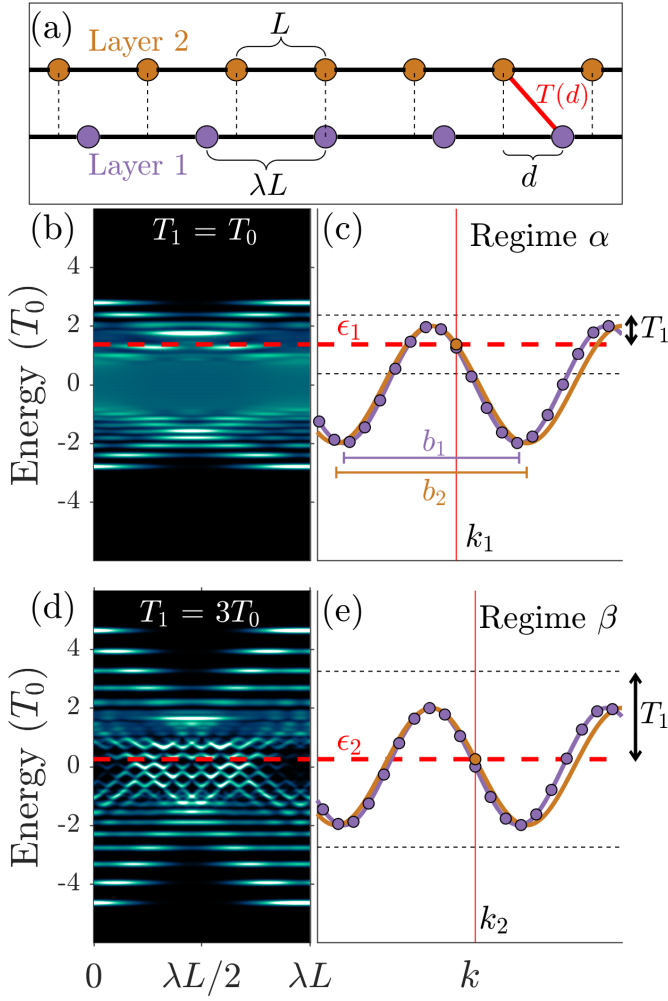


FIG. 3. (a) The 1D two-chain model, with relevant variables labeled. (b,d) Configuration-dependent LDoS of the two-chain system for two different interlayer coupling strengths, with a specific energy value of interest ϵ_i given by the dashed red line. (c,e) Band structure of layer 1 (2) shown as a purple (orange) line. A given Bloch state at k_i on layer 2 (orange circle) can couple to multiple Bloch states in layer 1 (purple circles) because of the difference in lattice parameter. The dotted lines identify states likely to be strongly coupled to states of energy ϵ_i (see text for details).

origin of both the real-space bands and the dispersionless states can be understood by taking advantage of the duality between configuration and momentum space, and the mathematical works that inspired our numerical approach also noted this relationship^{30,31}. We define two regimes of $k \cdot p$ modeling that emerge from this construction, and compare them to their real-space analogs. We use Latin letters (A, B) for real-space, and corresponding Greek letters (α, β) in momentum-space to label these regimes:

- A. a small TBH in real-space: apply a Bloch transformation on a finite system in a large unit cell, which gives dispersionless flat bands in the BZ at

each eigenvalue of the finite system (comparable to electronic states of a small molecule);

- B. an infinite (or very large) TBH in real-space: perform a Bloch transformation to compute the smoothly varying bands in the BZ (comparable to electronic bands of a crystal);

- α . a small $k \cdot p$ model in momentum-space: apply an inverse Bloch transformation, which gives dispersionless flat bands in configuration space at each eigenvalue of the finite $k \cdot p$ system (electronic states of a small “molecule” in momentum-space);

- β . an infinite (or very large) $k \cdot p$ model in momentum-space: perform an inverse Bloch transformation to compute smoothly varying bands in configuration space (electronic bands of a “crystal” in momentum-space).

For example, $T_1 = 3T_0$ in our 1D model produces both regime α and regime β (see Fig. 3(d)): regime β occurs if ϵ is within T_1 of both band edges, otherwise regime α occurs.

For tBLG, the Bloch states far from the Dirac-point are guaranteed to be much higher in energy, leading to a finite $k \cdot p$ model with only a few degrees of freedom (regime α). In this language, we interpret the van-Hove singularities of tBLG as the twist-dependent energy levels of an effective Bloch-state “molecule” and the magic-angles as a twist-tuned resonance of the “molecular” eigenstates. For tBLMS near the valence band edge, the two interacting parabolic bands produce regime α . This is visible near 0 eV in Fig. 1(a) at configuration κ . Far from the valence band-edge, the situation is not so straightforward since the bandstructure is much more complicated, leading to both regimes.

To illustrate further this interpretation, we investigate the LDoS behavior of tBLMS near -4.0 eV in Fig. 4. Here the important feature is again the effective number of degrees of freedom in the $k \cdot p$ model. At a twist angle of 5.0° , we return to the two previously defined energies in Fig. 1 and posit that E_1 corresponds to regime β , and E_2 to regime α . Similar to the 1D case, we will consider specific energy values of the single-layer bandstructure and analyze the *connectivity* of the energy landscape around these values. We define the connectivity as a width of energy around a value within which there are other states of similar character. This width around specific values is roughly given by the amplitude of the Fourier transform of the interlayer-coupling, which for this system’s p_z orbitals is $T_1 = 1.2$ eV. In 4(b,c), we plot the connectivity for the two energy regions. E_1 is a periodic, connected set and generates an infinite $k \cdot p$ model. The topology of E_2 is that of a small isolated disc, so it generates a finite $k \cdot p$ model. Thus, as the energy changes from E_1 to E_2 , smooth band-like features change slowly into localized energy levels. A thorough characterization of effective $k \cdot p$ models, and how to generate them directly

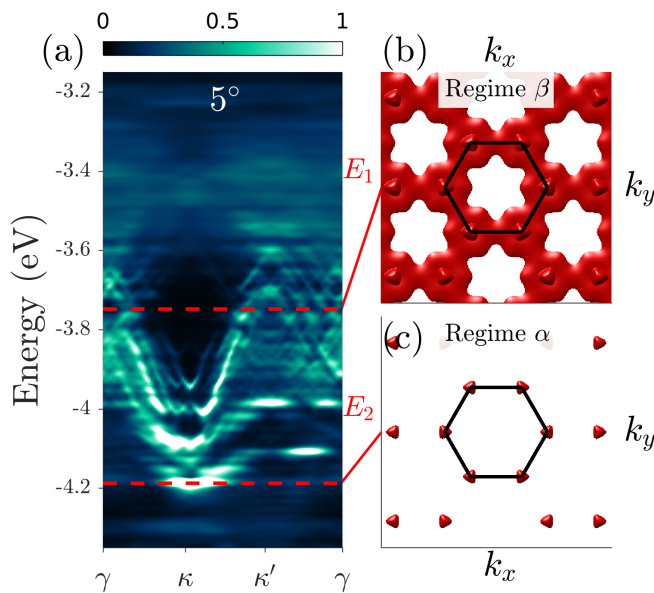


FIG. 4. (a) Configuration-dependent LDoS for tBLMS in the valence band at a twist angle of 5° . (b,c) Connectivity of the p_z projected bandstructure of single-layer MoSe₂ for two values of the energy $E_1 = -3.75$ eV and $E_2 = -4.19$ eV: the contours are created by taking all single-layer Bloch states within T_1 (1.2 eV) of the given energy value. The single-layer irreducible BZ is indicated by the black hexagon. These structures play the same role as the region within the dotted black lines in Fig. 3(c,e).

for all energy ranges from a given tight-binding model, has been reported in another work³². If the real-space banding leads to creation of localized electronic states, many-body effects may affect the predicted single-body electronic structure. This is not a shortcoming of the the-

ory presented here, but rather a starting point for a new many-body approach based on the single-body states we identify.

The real-space bands reported here may provide a new platform for studying quantum-dot physics and their applications. The localized electronic states in tBLG in regions with AA stacking are not a feature unique to that material, since similar features appear in the energy region 4 eV below the valence band edge in twisted bilayer MoSe₂, as shown in Fig. 1. Other twisted-bilayer materials may have more complicated electronic structure at the small twist-angle regime, such as the metallic (1T) phase of TMDCs. Importantly, the role of atomic relaxation in these twisted heterostructures^{33–35} is not included in the present work, but our approach can easily be extended to take into account such effects. The relaxations, viewed as frozen phonons, will cause additional momentum-scattering between Bloch states via electron-phonon coupling, and can be treated in either a tight-binding or $k \cdot p$ formalism. Many applications that take advantage of electron localization in these structures and its dependence on twist angle can be envisaged, such as arrays of quantum dots or networks of 1D electron channels.

ACKNOWLEDGMENTS

We acknowledge G. Kim, S. Fang, and P. Cazeaux for helpful discussions. Calculations were performed on the Odyssey cluster supported by the FAS Division of Science, Research Computing Group at Harvard University. This work was supported by the ARO MURI Award No. W911NF-14-0247.

- ¹ K. S. Novoselov, A. K. Geim, S. V. Morozov, D. Jiang, Y. Zhang, S. V. Dubonos, I. V. Grigorieva, and A. A. Firsov, *Science (New York, N.Y.)* **306**, 666 (2004).
- ² A. Ayari, E. Cobas, O. Ogundadegbe, and M. S. Fuhrer, *Journal of Applied Physics* **101**, 014507 (2007).
- ³ C. R. Dean, A. F. Young, I. Meric, C. Lee, L. Wang, S. Sorgenfrei, K. Watanabe, T. Taniguchi, P. Kim, K. L. Shepard, and J. Hone, *Nature nanotechnology* **5**, 722 (2010).
- ⁴ K. F. Mak, C. Lee, J. Hone, J. Shan, and T. F. Heinz, *Physical review letters* **105**, 136805 (2010).
- ⁵ B. Radisavljevic, A. Radenovic, J. Brivio, V. Giacometti, and A. Kis, *Nature nanotechnology* **6**, 147 (2011).
- ⁶ D. De, J. Manongdo, S. See, V. Zhang, A. Guloy, and H. Peng, *Nanotechnology* **24**, 025202 (2013).
- ⁷ B. Hunt, J. D. Sanchez-Yamagishi, A. F. Young, M. Yankowitz, B. J. LeRoy, K. Watanabe, T. Taniguchi, P. Moon, M. Koshino, P. Jarillo-Herrero, and R. C. Ashoori, *Science* **340**, 1427 (2013), <http://science.sciencemag.org/content/340/6139/1427.full.pdf>.
- ⁸ Y. Cao, J. Y. Luo, V. Fatemi, S. Fang, J. D. Sanchez-Yamagishi, K. Watanabe, T. Taniguchi, E. Kaxiras, and P. Jarillo-Herrero, *Physical Review Letters* **117**, 116804 (2016).
- ⁹ E. Koren, I. Leven, E. Lörtscher, A. Knoll, O. Hod, and U. Duerig, *Nature nanotechnology* **11**, 752 (2016).
- ¹⁰ K. Kim, A. DaSilva, S. Huang, B. Fallahazad, S. Larentis, T. Taniguchi, K. Watanabe, B. J. LeRoy, A. H. MacDonald, and E. Tutuc, *Proceedings of the National Academy of Sciences* **114**, 3364 (2017), <http://www.pnas.org/content/114/13/3364.full.pdf>.
- ¹¹ A. K. Geim and I. V. Grigorieva, *Nature* **499**, 419 (2013).
- ¹² G. Li, A. Luican, J. M. B. Lopes dos Santos, A. H. Castro Neto, A. Reina, J. Kong, and E. Y. Andrei, *Nature Physics* **6**, 109 (2009).
- ¹³ R. Bistritzer and A. H. MacDonald, *Proceedings of the National Academy of Sciences of the United States of America* **108**, 12233 (2011).
- ¹⁴ P. San-Jose, J. González, and F. Guinea, *Physical review letters* **108**, 216802 (2012).
- ¹⁵ D. Wong, Y. Wang, J. Jung, S. Pezzini, A. M. DaSilva,

- H.-Z. Tsai, H. S. Jung, R. Khajeh, Y. Kim, J. Lee, S. Kahn, S. Tollabimazraehno, H. Rasool, K. Watanabe, T. Taniguchi, A. Zettl, S. Adam, A. H. MacDonald, and M. F. Crommie, *Physical Review B* **92**, 155409 (2015).
- ¹⁶ I. Brihuega, P. Mallet, H. González-Herrero, G. Trambly de Laissardière, M. M. Ugeda, L. Magaud, J. M. Gómez-Rodríguez, F. Ynduráin, and J.-Y. Veuillen, *Physical review letters* **109**, 196802 (2012).
- ¹⁷ A. Luican, G. Li, A. Reina, J. Kong, R. R. Nair, K. S. Novoselov, A. K. Geim, and E. Y. Andrei, *Phys. Rev. Lett.* **106**, 126802 (2011).
- ¹⁸ C. Zhang, C.-P. Chuu, X. Ren, M.-Y. Li, L.-J. Li, C. Jin, M.-Y. Chou, and C.-K. Shih, *Science Advances* **3** (2017), 10.1126/sciadv.1601459, <http://advances.sciencemag.org/content/3/1/e1601459.full.pdf>.
- ¹⁹ K. Uchida, S. Furuya, J.-I. Iwata, and A. Oshiyama, *Physical Review B* **90**, 155451 (2014).
- ²⁰ J. M. B. Lopes dos Santos, N. M. R. Peres, and A. H. Castro Neto, *Physical review B* **86**, 155449 (2012).
- ²¹ P. Moon and M. Koshino, *Physical Review B* **87**, 205404 (2013).
- ²² Y.-i. Matsushita, H. Nishi, J.-i. Iwata, T. Kosugi, and A. Oshiyama, *Phys. Rev. Materials* **2**, 010801 (2018).
- ²³ E. J. Mele, *Phys. Rev. B* **81**, 161405 (2010).
- ²⁴ E. J. Mele, *Journal of Physics D: Applied Physics* **45**, 154004 (2012).
- ²⁵ A. Kormányos, G. Burkard, M. Gmitra, J. Fabian, V. Zolyomi, N. D. Drummond, and V. Falko, *2D Materials* **2**, 022001 (2015).
- ²⁶ S. Fang, R. Kuate Defo, S. N. Shirodkar, S. Lieu, G. A. Tritsarlis, and E. Kaxiras, *Physical Review B* **92**, 205108 (2015).
- ²⁷ S. Fang and E. Kaxiras, *Physical Review B* **93**, 235153 (2016).
- ²⁸ D. Massatt, M. Luskin, and C. Ortner, *Multiscale Modeling & Simulation* **15**, 476 (2017).
- ²⁹ S. Carr, D. Massatt, S. Fang, P. Cazeaux, M. Luskin, and E. Kaxiras, *Phys. Rev. B* **95**, 075420 (2017).
- ³⁰ J. Bellissard, A. van Elst, and H. Schulz-Baldes, *Journal of Mathematical Physics* **35**, 5373 (1994).
- ³¹ E. Prodan, *Applied Mathematics Research eXpress* **2**, 176 (2012).
- ³² D. Massatt, S. Carr, M. Luskin, and C. Ortner, *Multiscale Modeling & Simulation* (accepted) (2018).
- ³³ J. S. Alden, A. W. Tsen, P. Y. Huang, R. Hovden, L. Brown, J. Park, D. A. Muller, and P. L. McEuen, *Proceedings of the National Academy of Sciences* **110**, 11256 (2013), <http://www.pnas.org/content/110/28/11256.full.pdf>.
- ³⁴ S. Dai, Y. Xiang, and D. J. Srolovitz, *Nano Letters* **16**, 5923 (2016), pMID: 27533089, <http://dx.doi.org/10.1021/acs.nanolett.6b02870>.
- ³⁵ N. N. T. Nam and M. Koshino, *Phys. Rev. B* **96**, 075311 (2017).